



Contents lists available at ScienceDirect

## International Journal of Heat and Mass Transfer

journal homepage: [www.elsevier.com/locate/ijhmt](http://www.elsevier.com/locate/ijhmt)

# Numerical simulation of unsteady flows in Czochralski crystal growth by lattice Boltzmann methods

Haibo Huang<sup>a,\*</sup>, Xi-yun Lu<sup>a</sup>, Manfred Krafczyk<sup>b</sup><sup>a</sup> Department of Modern Mechanics, University of Science and Technology of China, Hefei, Anhui 230026, China<sup>b</sup> Institute for Computational Modeling in Civil Engineering, Technische Universität, Braunschweig 38106, Germany

## ARTICLE INFO

## Article history:

Received 21 April 2012

Received in revised form 12 July 2013

Accepted 3 March 2014

## Keywords:

Lattice Boltzmann

Thermal

Axisymmetric

Crystal growth

Convection–diffusion

## ABSTRACT

This study presents model extensions for a lattice Boltzmann (LB) approach to thermal axisymmetric flow including swirl or rotation. An incompressible axisymmetric lattice Boltzmann D2Q9 model was applied to solve the axial and radial velocities through inserting source terms into the two-dimensional lattice Boltzmann equation. The equations governing azimuthal (or swirling) velocity and the temperature were also solved by the LBM. It is found that this scheme is much more stable and consistent compared to previous hybrid schemes. It provides a significant advantage in simulation of melt flows with high Reynolds number and high Grashof number. The present scheme was validated by comparing the LB results with benchmark solutions for melt flow in Czochralski crystal growth. Unsteady flows with high Grashof numbers were studied in detail. The critical Grashof number for the onset of the oscillation is found to be about  $2.5 \times 10^6$ . The oscillation amplitude  $\psi_{max}$  is proportional to  $(Gr - Gr_c)^{0.5}$  for  $2.5 \times 10^6 < Gr < 6 \times 10^6$ . The frequencies and flow patterns of the unsteady flows are also analyzed. The distributions of the mean quantities of the temperature and rms of temperature at Grashof number as high as  $6 \times 10^7$  is found to be similar to those obtained by 3D simulations.

© 2014 Elsevier Ltd. All rights reserved.

## 1. Introduction

Many important engineering flows involve swirl or rotation, e.g., flows in combustion, turbomachinery and mixing tanks. Axisymmetric flows including swirl and thermal effects are more complex than isothermal axisymmetric flows without rotation since all these effects are all coupled non-linearly by the governing equations.

Melt flow in crystal growth systems is a complex flow system including swirling and thermal effects. Czochralski (CZ) crystal growth is one of the major prototypical systems for melt-crystal growth. Because the CZ crystal growth system is able to produce large single and perfect crystals, it has received substantial attention [1–4]. In typical CZ crystal growth systems, the high Reynolds and Grashof number of the melt make numerical simulation difficult due to the stiffness of the corresponding partial difference equations.

Conventional computational fluid dynamics (CFD) methods such as finite volume and finite difference methods have been developed to study flows in CZ crystal growth system [1–4]. In

the last two decades, the lattice Boltzmann (LB) method has been developed as an alternative numerical scheme for solving the incompressible Navier–Stokes (NS) equations. One main advantage of the LBM is that the convection operator of LBM in phase space is linear and exact which may be better than the discretization methods for the convection terms in conventional CFD methods [5–7].

The standard two-dimensional (2D) LBM is based on the Cartesian coordinate system. Hence, axisymmetric swirling flows can not directly be simulated as a quasi-three-dimensional problem in cylindrical coordinates using a standard 2D LBM. On the other hand, axisymmetric swirling flows can be simulated by the three-dimensional (3D) LBM [8] which uses 3D cubic lattices with proper curved wall boundary treatment directly. However, that implies a large grid size and is computationally expensive.

In 2001, Halliday et al. [9] proposed an axisymmetric D2Q9 model to simulate isothermal axisymmetric flows. The main idea of the model is to insert several spatial and velocity dependent “source” terms into the 2D lattice Boltzmann equation (LBE) [10–12]. Following the idea of Halliday et al. [9], Peng et al. [5] used a hybrid scheme to study the melt flow in CZ crystal growth. In this scheme, an axisymmetric D2Q9 LBM is used to solve the NS equation in cylindrical coordinates and the swirling velocity and the temperature are solved by a finite difference method.

\* Corresponding author. Tel.: +86 551 3603345.

E-mail address: [huanghb@ustc.edu.cn](mailto:huanghb@ustc.edu.cn) (H. Huang).

However, the axisymmetric model and hybrid scheme used by Peng et al. [5] and Huang et al. [6] is unstable for simulations of melt flows with high Reynolds number ( $Re = 10^4$ ) and high Grashof number ( $Gr = 10^7$ ) even with very fine grids. To improve the numerical stability, we propose that not only the NS equations but also the governing equation for the swirling velocity and temperature be solved by the LBM. This is more consistent and it results in improved numerical stability than the hybrid schemes.

The melt flows in CZ crystal growth system can be described by the NS equations and two convection diffusion equations (CDE). An incompressible axisymmetric LB model [13] is used for solving the NS equations. For solving the CDE, D2Q9, D2Q7, and D2Q5 models in literature are available [14–19]. Here a simple D2Q5 model is used for solving the CDE.

The scheme described below is qualitatively different from the method discussed by Chen et al. [19], who simulate the melt flow system by solving three CDEs and a Poisson equation. Usually, the LBM solves incompressible time-dependent NS equations more efficiently than the common explicit CFD methods because the Poisson equation is not required to be solved in the LBM. The present scheme does not require a Poisson equation to be solved and only two CDEs are required to be solved. Hence, the present scheme can be demonstrated to be more efficient than the scheme of Chen et al. [19].

Our LB scheme was initially validated by comparing the LBM results with the benchmark solutions for melt flow in Czochralski crystal growth [20]. Our numerical results were also compared with the data of Bansch et al. [21] and Nikitin et al. [2]. Numerical stability tests are also performed.

Although there are many studies on hydrodynamic stability phenomena in melt flow in CZ crystal growth [22], there are only very few specific numerical data to figure out a critical Grashof number where the temperature oscillations begin [2,22].

Here we focus on cases with high Grashof numbers. The flow patterns and frequencies of unsteady flows with high Grashof numbers was analyzed. The critical Grashof number for the onset of the oscillation and the behavior of oscillation amplitude were investigated in detail. The distributions of the mean quantities of the temperature and root-mean-square (rms) of temperature at high Grashof number were also investigated.

## 2. Numerical methods

### 2.1. Governing equations

The following continuity equation (Eq. (1)) and Navier–Stokes momentum equations (Eq. (2)) in pseudo-Cartesian coordinates ( $x, r$ ) are used to describe the laminar axisymmetric flow in axial and radial directions [23],

$$\partial_\beta u_\beta = -\frac{u_r}{r}, \quad (1)$$

$$\begin{aligned} \partial_t u_x + \partial_\beta (u_\beta u_x) + \frac{1}{\rho_0} \partial_x p - \nu \partial_\beta (\partial_\beta u_x) \\ = -\frac{u_x u_r}{r} + \frac{\nu}{r} \left( \partial_r u_x - \frac{u_r}{r} \delta_{xr} \right) + \frac{u_\theta^2}{r} \delta_{xr} + Q, \end{aligned} \quad (2)$$

where  $u_\beta (\beta = x, r)$  are the two components of velocity;  $u_x$  is the velocity  $u_x$  or  $u_r$ ;  $\nu$  is the kinematic viscosity. The symmetry axis is in  $x$  direction.  $Q$  is an additional source term that may appear in some flow problems. In the above equations we adopt the Einstein summation convention.

For axisymmetric swirling flows, there are no circumferential gradients but there may still be non-zero swirling velocities  $u_\theta$ . The momentum equation of azimuthal velocity is

$$\partial_t u_\theta + \partial_\beta (u_\beta u_\theta) = \nu \partial_\beta (\partial_\beta u_\theta) + \frac{\nu}{r} \left( \partial_r u_\theta - \frac{u_\theta}{r} \right) - 2 \frac{u_r u_\theta}{r}. \quad (3)$$

In Eq. (2), the Boussinesq approximation is applied to the buoyancy force term  $Q = g \gamma_0 (T - T_c) \delta_{xx}$ , where  $g$  is the acceleration due to gravity;  $\gamma_0$  is the thermal expansion coefficient;  $T_c$  is the temperature of crucible (refer to Fig. 1). The governing equation of temperature is

$$\partial_t T + \partial_\beta (u_\beta T) = k_0 \partial_\beta (\partial_\beta T) + G, \quad (4)$$

where the Prandtl number  $Pr$  is defined as  $Pr = \frac{\nu}{k_0}$  and  $k_0$  is the thermal diffusion constant. In the above equation,  $G = \frac{\nu}{Pr} \frac{1}{r} \partial_r T - T \frac{u_r}{r}$ , which can be regarded as a source term.

### 2.2. Axisymmetric lattice Boltzmann method

In our study we use an axisymmetric lattice Boltzmann D2Q9 model [13], which is derived from an incompressible LBGK D2Q9 model [24]. The evaluation equation to describe 2D flow in  $(x, r)$  pseudo-Cartesian coordinates is Eq. (5), which is similar to the evaluation equation for standard D2Q9 model in 2D  $(x, y)$  Cartesian coordinates. The difference is that a source term  $H_i^{(1)}$  and  $H_i^{(2)}$  were incorporated into the microscopic evolution equation.

$$\begin{aligned} f_i(x + e_{ix} \delta_t, r + e_{ir} \delta_t, t + \delta_t) - f_i(x, r, t) \\ = \frac{1}{\tau} [f_i^{eq}(x, r, t) - f_i(x, r, t)] + \delta_t H_i^{(1)}(x, r, t) + \delta_t H_i^{(2)}(x, r, t) \end{aligned} \quad (5)$$

In Eq. (5),  $f_i(x, r, t)$  are the distribution functions for particles with velocity  $\mathbf{e}_i$  at position  $(x, r)$  and time  $t$ . The 9 discrete velocities  $\mathbf{e}_i$  are given by  $\mathbf{e}_0 = (0, 0)$ ,  $\mathbf{e}_i = c(\cos(i-1)\frac{\pi}{2}, \sin(i-1)\frac{\pi}{2})$ ,  $i = 1, 2, 3, 4$ , and  $\mathbf{e}_i = \sqrt{2}c(\cos((i-5)\frac{\pi}{2} + \frac{\pi}{4}), \sin((i-5)\frac{\pi}{2} + \frac{\pi}{4}))$ ,  $i = 5, 6, 7, 8$ , where  $c = \delta_x / \delta_t$ .  $\delta_x$  and  $\delta_t$  are the lattice spacing ( $l.u.$ ) and time step size ( $t.s.$ ). In our studies  $c \equiv 1 l.u./t.s.$   $H_i^{(1)}$  and  $H_i^{(2)}$  are the “source” terms added to the collision operator. They are responsible to recover the extra terms in the continuity equation (Eq. (1)) and momentum equations (Eq. (2)), respectively [13]. The non-dimensional relaxation time constant  $\tau$  and the fluid viscosity satisfies  $\nu = c_s^2 \delta_t (\tau - 0.5)$ , where  $c_s = c/\sqrt{3}$ . In Eq. (5), the equilibrium distribution functions (EDF)  $f_i^{eq}$  of the incompressible D2Q9 model are given [24]

$$f_i^{eq}(x, r, t) = \omega_i \frac{p}{c_s^2} + \omega_i \rho_0 \left[ \frac{\mathbf{e}_i \cdot \mathbf{u}}{c_s^2} + \frac{(\mathbf{e}_i \cdot \mathbf{u})^2}{2c_s^4} - \frac{\mathbf{u}^2}{2c_s^2} \right], \quad i = 0, 1, 2, \dots, 8. \quad (6)$$

$p$  is the hydrodynamic pressure and  $\rho_0$  is the density of fluid. In the above equations,  $\omega_0 = 4/9$ ,  $\omega_i = 1/9$ , ( $i = 1, 2, 3, 4$ ),  $\omega_i = 1/36$ , ( $i = 5, 6, 7, 8$ ). They are nondimensional parameters.

The pressure  $p$  and momentum  $\rho_0 u$  are defined as:

$$\frac{p}{c_s^2} = \sum_i f_i = \sum_i f_i^{eq}, \quad \rho_0 u_x = \sum_i e_{ix} f_i + \frac{1}{2} \rho_0 F_x \delta_t, \quad (7)$$

where  $F_x$  represents the acceleration of a body force or source term in the momentum equations and has the unit of  $l.u./t.s.$ <sup>2</sup>.

In order to recover the extra terms,

$$F_x = \left[ -\frac{u_x u_r}{r} + \frac{\nu}{r} \left( \partial_r u_x - \frac{u_r}{r} \delta_{xr} \right) + \frac{u_\theta^2}{r} \delta_{xr} + Q \right], \quad (8)$$

in the 2-D NS equations, the following source terms should be added into the lattice Boltzmann equation [13,25]

$$H_i^{(1)} = -\frac{\omega_i \rho_0 u_r}{r}, \quad (9)$$

$$H_i^{(2)} = \left( 1 - \frac{1}{2\tau} \right) F_x \frac{(e_{ix} - u_x)}{c_s^2} f_i^{eq}.$$

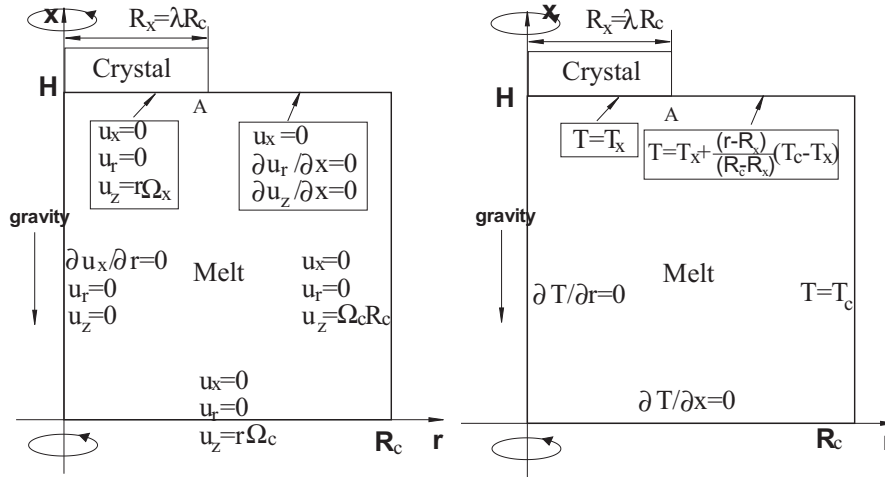


Fig. 1. The momentum and thermal boundary conditions of melt flow in Czochralski crystal growth.

For the velocity derivatives in the above equations, the term  $\partial_r u_x + \partial_x u_r$  can be obtained through Eq. (10),

$$\rho_0 v (\partial_x u_r + \partial_r u_x) = - \left( 1 - \frac{1}{2\tau} \right) \sum_{i=0}^8 f_i^{ne} e_{ix} e_{ir}, \quad (10)$$

where  $f_i^{ne} = f_i - f_i^{eq}$ . Similarly,  $\partial_x u_x = -\frac{1}{2\rho_0 v} \left( 1 - \frac{1}{2\tau} \right) \sum_{i=0}^8 f_i^{ne} e_{ix} e_{ix}$ , and  $\partial_r u_r = -\frac{1}{2\rho_0 v} \left( 1 - \frac{1}{2\tau} \right) \sum_{i=0}^8 f_i^{ne} e_{ir} e_{ir}$ . The term  $\partial_r u_x$  in the source terms is equal to  $(\partial_r u_x + \partial_x u_r) - \partial_x u_r$ . Since  $(\partial_r u_x + \partial_x u_r)$  can be easily obtained by Eq. (10), only the value of  $\partial_x u_r$  is left unknown to determine  $\partial_r u_x$ . Here a finite difference method is used to obtain  $\partial_x u_r$  at lattice node  $(i, j)$ , which can be calculated by  $(\partial_x u_r)_{ij} \approx ((u_r)_{i+1,j} - (u_r)_{i-1,j}) / (2\delta_x)$ .

The values of  $\partial_r u_x + \partial_x u_r$ ,  $\partial_x u_x$ ,  $\partial_r u_r$ ,  $\partial_r u_x$  and  $\partial_x u_r$  for the lattice nodes on the wall boundary can also be calculated from Eq. (10) and a one sided finite-difference scheme. Hence, for the additional source term in our model, most velocity gradient terms can be obtained from second order moments of non-equilibrium distribution functions, which is consistent with the philosophy of the LBM.

### 2.3. Lattice Boltzmann methods for CDE

He and Luo have shown that the LB equation can be derived from the Boltzmann equation [26]. Since the hydrodynamic moments of  $f_i^{eq}$  can be evaluated by quadrature formulas, the 2D velocity space  $\xi$  is discretized into several finite velocities  $\mathbf{e}_i$  [26]. To solve the 2D NS equations, a D2Q9 velocity model with 9 velocities is necessary for a Cartesian coordinate lattice [26]. However, to recover a CDE, the derivation of the CDE from the LBE shows that fourth-order isotropic lattice tensors are not required. Hence, models with fewer velocities, e.g., D2Q5 and D2Q4, can be used [15,32–34].

In the following part, we illustrate how to solve a typical CDE (Eq. (4)) using LBM. In many studies [14,16,17,19], when the LB method is used to solve a CDE, a common LBE in the form of Eq. (11) is used.

$$\mathbf{g}_i(\mathbf{x} + \mathbf{e}_i \delta t, t + \delta t) - \mathbf{g}_i(\mathbf{x}, t) = \frac{1}{\tau_g} [\mathbf{g}_i^{eq}(\mathbf{x}, t) - \mathbf{g}_i(\mathbf{x}, t)] + \delta_t S_i. \quad (11)$$

In Eq. (11),  $\tau_g$  is a nondimensional relaxation time constant and  $S_i$  is a source term used to recover the source term  $G$  in Eq. (4). The EDF,  $\mathbf{g}_i^{eq}$ , has different forms in the studies referenced above.

The EDF of  $f_i^{eq}$  relevant to NS equations (i.e., Eq. (2)) involves terms of  $O(u^2)$ . However, the solution of the CDE does not require

second-order velocity terms; keeping only terms of  $O(u)$  in the EDF has been proven consistent with the second-order spatial accuracy of LBM [27]. Here we adopt this strategy and in the EDF of the following models, only terms of  $O(u)$  are retained. Keeping terms of  $O(u)$  in the EDF and through the derivative procedure from Boltzmann equation to LB equation [26], we can obtain a general formula for weighting factors in EDF is

$$\mathbf{g}_i^{(0)} = B_i T + \frac{T e_{ix} u_x}{2c^2} \quad (12)$$

with  $B_0 = 1 - 2\eta_g$ ,  $B_i = \frac{1}{2}\eta_g$ ,  $i = 1, 2, 3, 4$ , where  $\eta_g \in (0, 0.5)$  is a free, positive, and nondimensional parameter determined by the equation  $k_0 = c^2 (\tau_g - 0.5) \eta_g \delta_t$ .  $T$  is obtained from  $T = \sum_i g_i$ . We note that when  $\eta_g = 0.5$ , Eq. (12) becomes a D2Q4 model formula.

There are some specific cases of the above general formula in the literature. In the study of Huber et al. [18],  $\mathbf{g}_i^{eq} = W_i T \left[ 1 + \frac{\mathbf{e}_i \cdot \mathbf{u}}{c^2} \right]$ . The weighting factor  $W_0 = \frac{1}{3}$  and  $W_i = \frac{1}{6}$ ,  $i = 1, 2, 3, 4$ . Hence, the formula of the EDF can be written as  $\mathbf{g}_i^{eq} = W_i T + \frac{T}{2c^2} (\mathbf{e}_i \cdot \mathbf{u})$  due to  $\mathbf{e}_0 = (0, 0)$ . In the study of Chen et al. [19], the EDF is given by  $\mathbf{g}_i^{eq} = \frac{T}{5} + \frac{T}{2c^2} (\mathbf{e}_i \cdot \mathbf{u})$ ,  $i = 0, 1, 2, 3, 4$ .

In Eq. (4),  $G = \frac{v}{Pr} \left( \frac{1}{r} \partial_r T \right) - T \frac{u_r}{r}$ . To mimic Eq. (4) correctly, through Chapman-Enskog expansion we obtained the constraints of  $S_i$  in Eq. (11):  $G = \sum_i S_i$  and  $\sum_i e_{ip} S_i = 0$ . For convenience,  $S_i$  take the form  $S_i = 0.25 G$ ,  $i = 1, 2, 3, 4$  in our LBM simulations, which satisfy the constraints.

To solve the momentum equation of azimuthal velocity, i.e., Eq. (3), the third LBE can be written as

$$h_i(\mathbf{x} + \mathbf{e}_i \delta t, t + \delta t) - h_i(\mathbf{x}, t) = \frac{1}{\tau_h} [h_i^{eq}(\mathbf{x}, t) - h_i(\mathbf{x}, t)] + \delta_t S_i \quad (13)$$

where  $h_0^{eq} = (1 - 2\eta_h) u_\theta$  and  $h_i^{eq} = \frac{\eta_h}{2} u_\theta + \frac{u_\theta e_{iz} u_z}{2c^2}$ ,  $i = 1, 2, 3, 4$ .  $\eta_h \in (0, 0.5)$  is a free, positive, and nondimensional parameter.  $\tau_h$  satisfies the constraint  $v = c^2 (\tau_h - 0.5) \eta_h \delta_t$ .  $u_\theta$  is obtained from  $u_\theta = \sum_i h_i$ . The source term can take the form  $S_i = 0.25 \left( \frac{v}{r} (\partial_r u_\theta - \frac{u_\theta}{r}) - 2 \frac{u_r u_\theta}{r} \right)$ .

### 3. Boundary conditions:

Boundary conditions are an important issue when using the LBM to simulate fluid flows. The no-slip boundary conditions can be handled by the momentum exchange scheme [30], bounce-back or modified bounce-back [29], or the non-equilibrium bounce-back scheme [31]. Here in our study, the modified bounce-back scheme

[29] was adopted to handle the no-slip boundary. In this scheme, collision and forcing still occur at boundary nodes, which is also consistent with the momentum exchange scheme [30]. For the four corner points in our simulations, the scheme proposed by Zou and He [31] was applied. For example, in the left lower corner point  $\mathbf{x}$ , the unknown distribution functions  $f_1, f_2, f_3, f_5$  and  $f_8$  are obtained from  $f_1 = f_3, f_2 = f_4, f_5 = f_7,$  and  $f_6 = f_8 = 0.5(\rho(\mathbf{x} + \mathbf{e}_5) - f_0 - 2(f_3 + f_4 + f_7))$ . This is implemented just after the streaming step and before the collision step.

For the axisymmetric boundary condition (i.e., the  $x$ -axis), the specular reflection scheme was applied to lattice nodes in axis [5]. The specular reflection scheme can be applied to model the free-slip boundary condition where no tangential momentum is being exchanged with the boundary. Hence, for the free surface (e.g.,  $x = H, R_x < r < R_c$  in our setup depicted in Fig. 1), the specular boundary condition is also applied.

For the boundary conditions of the CDE, two types of boundary conditions are used, simple bounce-back and revised regularized scheme [28]. In simulations including a Neumann type boundary, the bounce-back scheme is applied while when the macroscopic variable  $T$  or  $u_w$  are specified in the boundary, the revised regularized scheme is applied. The simple bounce-back used here means the standard collision process does not occur on the boundary. In contrast, the regularized scheme implies that the collision process on the boundary node is still implemented and the idea of “bounce back of opposite value of off-equilibrium parts” is adopted [28].

## 4. Results and Discussion

### 4.1. Validation

In CZ crystal growth, the melt flow is very complex because it is a combination of natural convection due to thermal gradients and forced convection induced by rotation of the crystal and the crucible. Here, the Wheeler benchmark problem [20] in Czochralski crystal growth is used as a test case to validate the numerical method. The configuration and the momentum and thermal boundary conditions are all illustrated in Fig. 1. In the problem, a vertical cylindrical crucible filled with a melt to a height  $H = R_c$  rotates with an angular velocity  $\Omega_c$ . The top of the melt is bounded by a coaxial crystal with radius  $R_x = \lambda R_c$  ( $\lambda = 0.4$ ) which rotates with angular velocity  $\Omega_x$ . There is a phase boundary between the crystal and melt. In the top right part of the melt ( $R > R_x$ ), there is a free surface.  $u_x, u_r, u_\theta$  are the axial, radial and azimuthal velocities respectively.

The dimensionless parameters are Reynolds number  $Re_c, Re_x$ , Prandtl number  $Pr$  and Grashof number  $Gr$  are defined as

$$Re_c = \frac{R_c^2 \Omega_c}{\nu}, \quad Re_x = \frac{R_x^2 \Omega_x}{\nu}, \quad Pr = \frac{\nu}{k_0}, \quad Gr = \frac{g \gamma_0 (T_c - T_x) R_c^3}{\nu^2}.$$

In our simulations,  $Pr = 0.05$ . The parameters can be determined in the following ways. When a case of  $Gr \neq 0$  is simulated, a characteristic velocity  $U_t = \sqrt{g \gamma_0 (T_c - T_x) R_c}$  was defined, which may represent the maximum magnitude of the velocity in the flow field. Due to the incompressibility flow, we set  $U_t = 0.15 \text{ l.u./t.s.}$  Although here  $U_t$  represents the maximum magnitude of the velocity, in fact, in all of our simulation results, the maximum velocity is always less than  $U_t$ . Then,  $\nu$  can be determined from a given  $Gr$  because  $Gr = \frac{U_t^2 R_c^3}{\nu^2}$ . Hence, the other parameters, such as  $k_0, \tau$ , can all be determined. For example, in the cases of  $Gr = 2.5 \times 10^6, R_c = 100 \text{ l.u.}, \nu = 0.009487 \text{ l.u.}^2/\text{t.s.}, \tau = \frac{\nu}{c^2 \delta_t} + 0.5 = 0.5285$ . From  $Pr = 0.05$ , we get  $k_0 = 0.1897 \text{ l.u.}^2/\text{t.s.}$  If the free parameter  $\eta_g = \eta_h = 0.5$ , then  $\tau_g = \frac{k_0}{\eta_g c^2 \delta_t} + 0.5 = 0.8795$  and  $\tau_h = \frac{\nu}{\eta_h c^2 \delta_t} + 0.5 = 0.5190$ .

For  $Gr = 0$ , the parameters are determined in another way. First a characteristic velocity  $U_h = R_c \Omega_x \lambda = \frac{\nu}{R_c} Re_x \lambda$  is used and is usually set as  $0.15 \text{ l.u./t.s.}$ , then parameters such as  $\nu, \tau$ , etc. can be calculated.

In our simulations, zero velocity and zero temperature were initialized in the whole computational domain and the convergence criterion in our simulation is set to

$$\frac{\sum_{ij} \|\mathbf{u}(x_i, r_j, t - \Delta t) - \mathbf{u}(x_i, r_j, t)\|^2}{\sum_{ij} \|\mathbf{u}(x_i, r_j, t)\|^2} < 10^{-6}, \quad (14)$$

where the summation is over the entire system.  $\Delta t$  is usually set to  $5000 \text{ t.s.}$  in most of our simulations.

The stream function in the simulations,  $\psi$  is defined as

$$\frac{\partial \psi}{\partial r} = -r u_x, \quad \frac{\partial \psi}{\partial x} = r u_r, \quad (15)$$

with  $\psi = 0$  on the all boundaries of the computational domain. In the following sections, The nondimensional temperature is defined as  $T' = \frac{T - T_x}{T_c - T_x}$ , where  $T_x$  is the temperature of the crystal.  $R_c$ , and  $\frac{\nu}{R_c}$  are used as the length and velocity scales to normalize the dimensional values, for example, the stream function is normalized by  $\psi = \psi_{LB} / \frac{\nu}{R_c} R_c^2$ , where  $\psi_{LB}$  is the stream function value in lattice units. The minimum and maximum values of stream function denoted by  $\psi_{min}$  and  $\psi_{max}$  are used to compare the results of our scheme with available data in the literature [21].

Initially, the grid independence of the results was examined. We choose the case A2 as an example. In this case,  $Gr = 0, Re_x = 10^3$ , and  $Re_c = 0$ . The  $\psi_{min}$  and  $\psi_{max}$  are compared to the result of Bansch et al. [21] in Table 1. In this table, we can see that  $100 \times 100$  grid is sufficient to obtain accurate results.

We also investigated whether  $\tau_g$  and  $\tau_h$  would affect the numerical results even when  $\tau$  is fixed. Table 2 shows that if  $\tau_g$  is not too large ( $\tau_g < 2.0$ ), the discrepancy of  $\psi_{max}$  between our numerical results and Bansch et al. [21] are less than 1%. Hence, when  $\tau_g$  is not much larger than unity, the choice of parameters  $\tau_g$  and  $\tau_h$  in our numerical scheme will not affect the accuracy of the results. The numerical error of the velocity field (defined in Eq. (14)) as a function of time steps are also illustrated in Fig. 2. For the error calculation we chose  $\Delta t = 500 \text{ t.s.}$  It seems that the convergence behavior of all cases are similar and results for cases 1–3 are almost identical.

Secondly, as many as 11 cases with difference parameter sets were simulated. The 11 cases were classified into four groups. In group A, the crystal rotates with  $Re_x$  varying from  $10^2$  to  $10^3$ , while the crucible is at rest with  $Gr = 0$ . In group B, the crystal and crucible rotate in opposite direction. Group A and B are all forced convection problems. The cases in group C are natural convection problems. In the cases of group D, the melt flows combined both the natural convection and forced convection were investigated which are more related to practical applications.

Table 3 shows the comparison of the computed minimum and maximum stream function values for 11 cases. A  $200 \times 200$  grid was used in the simulation of cases A3 and B3. The grid used in the other simulations is  $100 \times 100$ . For comparison, we also present the results of Buckle et al. [1] using the finite volume method. In

**Table 1**  
Grid dependence tests for Case A2 with  $Gr = 0, Re_x = 10^3$ , and  $Re_c = 0$ .

Grid	$\psi_{min}$	$\psi_{max}$
50 × 50	-5.3981	$4.6496 \times 10^{-5}$
100 × 100	-5.0332	$3.9064 \times 10^{-5}$
150 × 150	-5.1812	$8.7524 \times 10^{-5}$
200 × 200	-5.1656	$8.9199 \times 10^{-5}$
Ref. [21]	-5.1492	$4.8799 \times 10^{-4}$

**Table 2**

Parameter dependence of  $\tau_g, \tau_h$  for case C2,  $Gr = 10^6$ ,  $Re_x = 0$ , and  $Re_c = 0$  with grid size  $100 \times 100$ .

case	$\tau_g$	$\tau_h$	$\eta_g, \eta_h$	$\psi_{min}$	$\psi_{max}$
1	1.10	0.530	0.500	-0.31246	93.426
2	1.40	0.545	0.333	-0.34608	93.430
3	2.00	0.575	0.200	-0.46462	93.446
4	3.50	0.650	0.100	-1.0216	93.665
5	6.50	0.800	0.050	-2.2113	94.750
Ref. [21]	—	—	—	-0.27504	92.874

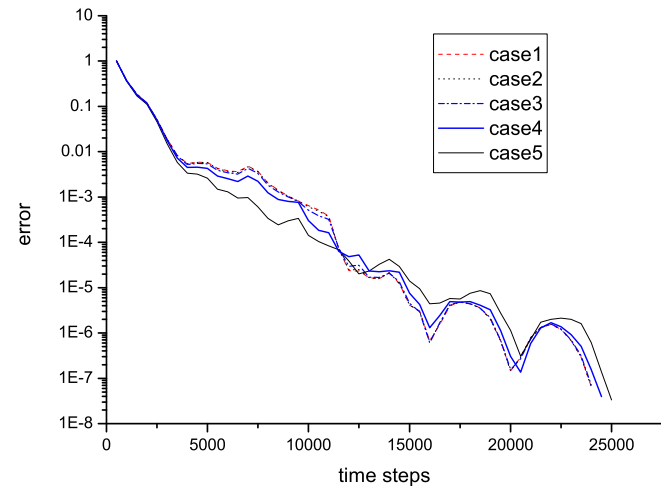


**Fig. 2.** The convergence behavior of the numerical error of velocity field for the C2 case with different  $\tau_g$  and  $\tau_h$ .

**Table 3**, the relative difference between our results and those of Buckle et al. [1] are also illustrated. The relative difference is defined as:  $d_{rel} = \frac{|(\psi_{max})_{LB} - (\psi_{max})_B| + |(\psi_{min})_{LB} - (\psi_{min})_B|}{|(\psi_{max})_B| + |(\psi_{min})_B|}$ . The subscript 'LB' and 'B' means the results of LBM and those of Buckle et al. [1]. Noted in the cases A1 and B1, the original  $\psi_{min}$  in Ref. [1] were misprinted [21].

From the table, we can see for the A3 case, the discrepancy of our LBM result and that of the Buckle et al. [1] is about 17%. This is large but is more consistent with the result of Bansch et al. [21]. In their result, for the case A3,  $\psi_{min}$  and  $\psi_{max}$  are  $-4.2262 \times 10^1$  and  $1.7701 \times 10^{-1}$ , respectively. Almost in all of the other 10 cases, the maximum absolute values of the stream function computed by the LBM agree very well with those of Buckle et al. [1] and Bansch et al. [21]. The discrepancies between our results and Buckle et al. [1] are usually less than 8%.

For the cases in group A, there is a primary vortex induced by rotation of the crystal and the intensity of the corresponding vor-

**Table 4**

Numerical stability comparison for case A1 and C1, grid  $100 \times 100$ .

case	$\tau_{min}$ (Present)	$\tau_{min}$ ([8])	$\tau_{min}$ ([5])
A1	$0.515 \pm 0.005$	$0.625 \pm 0.013$	$0.725 \pm 0.037$
C1	$0.512 \pm 0.005$	$0.606 \pm 0.008$	$0.671 \pm 0.013$

tex (represented by  $\psi_{max}$ ) with the Reynolds number of crystal. For the cases in group A with a higher Reynolds number, the center of the vortex moves towards the side wall of the crucible. For the cases in group B, the crystal and crucible rotate in opposite directions. As a result, there are two vortices with opposite directions appearing in the upper left corner just below the crystal and the lower right corner. The positions of the vortices change with the Reynolds number. In the natural convection flow cases of group C, the crucible and the crystal are all at rest. There is a primary vortex induced by the temperature difference between the crystal and the crucible. In the cases of group D, when  $Re_x < 10^3$ , the natural convective flow dominates the melt flow while the force convective flow induced by the crystal only has a minor effect.

#### 4.2. Numerical stability comparison

The numerical stability of the LBM depends on the relaxation time  $\tau$ , the Mach number of the flow and the size of mesh. In the LBM, if  $\tau$  is very close to 0.5, numerical instabilities may appear and  $\tau_{min}$  is usually case-dependent. The Reynolds number is usually defined as  $Re = \frac{U D}{\nu} = \left(\frac{U}{c_s}\right) \left(\frac{c}{c_s}\right) \left(\frac{D}{\delta_x}\right) \frac{1}{(\tau - 0.5)}$  and the Mach number in the LBM should obey  $\frac{U}{c_s} \ll 1$ . To simulate the cases of high Reynolds number, with limitation of  $\tau_{min}$  and Mach number, usually we have to increase the value of  $\frac{D}{\delta_x}$  (i.e., enlarge the grid size).

Compared with the previous LBM scheme [5,6], the present scheme solves the whole flow system by LBM as opposed to the hybrid method. It is more consistent and shows increased numerical stability as demonstrated below.

To compare the numerical stability of our method and previous models [5,6], the benchmark case A1 and C1 of melt flow in CZ crystal growth were also simulated using their hybrid methods with the same boundary condition treatment. Numerical stability can be demonstrated by computing the minimum  $\tau$  value at which numerical instability does not appear. For case A1, the characteristic velocity  $U_h$  is decreasing to measure the minimum  $\tau$  when the numerical simulations are still stable. For the case C1, the  $Gr$  number in the simulations is  $10^6$ . Then  $U_r$  is being reduced to see when the numerical instability appears. The  $\tau_{min}$ s for these schemes are listed in Table 4. From Table 4, we can see that in all cases,  $\tau_{min}$  of the present scheme are smaller than those of Peng et al. [5] and Huang et al. [6]. We conclude that our LB scheme is much more stable than the hybrid schemes [5,6].

**Table 3**

Results for the 11 test cases obtained by the LBM and the finite volume method [1].

Case	$Gr$	$Re_x$	$Re_c$	$\psi_{min}$	$\psi_{max}$	$\psi_{min}$ (Ref. [1])	$\psi_{max}$ (Ref. [1])	$d_{rel}$ (%)
A1	0	$10^2$	0	$-2.3537 \times 10^{-1}$	$5.4058 \times 10^{-6}$	$-2.3447 \times 10^{-1}$	$1.5642 \times 10^{-6}$	3.13
A2	0	$10^3$	0	$-5.0332 \times 10^0$	$3.9064 \times 10^{-5}$	$-5.3642 \times 10^0$	$1.5257 \times 10^{-4}$	6.17
A3	0	$10^4$	0	$-4.7296 \times 10^1$	$5.5884 \times 10^{-1}$	$-4.0443 \times 10^1$	$1.9320 \times 10^{-1}$	17.76
B1	0	$10^2$	-25	$-5.1457 \times 10^{-2}$	$1.1449 \times 10^{-1}$	$-5.0203 \times 10^{-2}$	$1.1796 \times 10^{-1}$	2.81
B2	0	$10^3$	-250	$-1.5532 \times 10^0$	$1.1108 \times 10^0$	$-1.6835 \times 10^0$	$1.2414 \times 10^0$	8.93
B3	0	$10^4$	-2500	$-8.3532 \times 10^0$	$4.8137 \times 10^0$	$-8.5415 \times 10^0$	$5.2708 \times 10^0$	4.67
C1	$10^5$	0	0	$-5.0760 \times 10^{-3}$	$2.8599 \times 10^1$	$-1.1936 \times 10^{-3}$	$2.8437 \times 10^1$	0.58
C2	$10^6$	0	0	$-3.3935 \times 10^{-1}$	$9.3592 \times 10^1$	$-3.9699 \times 10^{-1}$	$9.2100 \times 10^1$	1.68
D1	$10^5$	$10^1$	0	$-5.6875 \times 10^{-3}$	$2.8816 \times 10^1$	$-4.7057 \times 10^{-3}$	$2.8420 \times 10^1$	1.41
D2	$10^5$	$10^2$	0	$-5.6847 \times 10^{-3}$	$2.8794 \times 10^1$	$-4.7092 \times 10^{-4}$	$2.8393 \times 10^1$	1.43
D3	$10^5$	$10^3$	0	$-6.6822 \times 10^{-1}$	$2.4938 \times 10^1$	$-6.5631 \times 10^{-1}$	$2.4829 \times 10^1$	0.47

Thus our LB scheme provides a significant advantage in simulating melt flow cases with high Reynolds number and high Grashof number for a given mesh resolution.

### 4.3. Flow behavior at high Grashof number

Compared to the full 3D simulations, the 2D axisymmetric simulations predict a later onset of oscillations and stochastic flow [2]. However, even for  $Gr$  as high as  $6 \times 10^7$ , which is of practical interest, for the mean temperature and root-mean-square temperature oscillation field, there is only a slight discrepancy between the results of the 2D axisymmetric and 3D simulations [2]. Hence, the axisymmetric simulation in high Grashof number still captures the main flow characteristics.

Here we used the LBM to investigate the unsteady behavior in the melt flow in Czochralski crystal growth for high  $Gr$ . Using the grid  $100 \times 100$ , we obtained accurate results for cases with  $Gr$  around  $10^6$ .

Fig. 3 shows the oscillation of  $\psi_{max}$  in the flow field for cases  $Gr = 2.4 \times 10^6$ ,  $2.5 \times 10^6$ , and  $2.6 \times 10^6$  as functions of time. The time is a nondimensional value,  $t = \frac{t_{LB} v}{R_c^2}$ , where  $t_{LB}$  is the time steps in LBM simulations. We can see that for the case of  $Gr = 2.4 \times 10^6$ ,  $\psi_{max}$  finally becomes a constant, indicating the flow is in the steady-state regime. When the Grashof number increases to  $2.5 \times 10^6$  and  $2.6 \times 10^6$ , the flows are entering a periodic regime. The critical Grashof number  $Gr_c$  for this transition is about  $2.5 \times 10^6$ . The oscillation amplitude of  $\psi_{max}$  in the latter two cases are 0.15 and 1.49, respectively.

We also observed that the oscillation amplitude of the  $\psi_{max}$  is proportional to  $(Gr - Gr_c)^{0.5}$  when  $(Gr_c < Gr < 6 \times 10^6)$ . Our results are illustrated in Fig. 4. The linear fit of the data shows  $\delta\psi_{max} = 0.00666(Gr - Gr_c)^{0.5} - 0.522$ , where  $\delta\psi_{max}$  is the oscillation amplitude of  $\psi_{max}$ . (See Fig. 4).

Fig. 5 shows the oscillations of the temperature at the point ( $r = 0.64, x = 0.5$ ). When  $(Gr_c < Gr < 6 \times 10^6)$ , the mean temperature distribution of these periodic flows and that in the steady flow regime ( $Gr < Gr_c$ ) are similar. The difference is that the temperature and velocities are oscillating harmonically around a mean value at each point in the computational domain. For the cases of  $Gr = 7 \times 10^6$  and  $7.5 \times 10^6$ , multiple-harmonic amplitudes become significant. For larger  $Gr$  (the curves 4, 5, 6 in Fig. 5), the oscillations become very complex. For such high  $Gr$  cases, it is hard to distinguish one or multiple main frequencies from our analysis of the frequency spectra. In these high  $Gr$  cases the flows become chaotic.

By analysis of the frequency spectra, one or multiple main frequencies are obtained for cases  $Gr < 10^7$ . The details are listed in Table 5. We can see that when  $Gr_c < Gr < 6 \times 10^6$ , there is only one main frequency in the flow which increases monotonically from 3047 to 4356. In the case of  $Gr = 7.0 \times 10^6$ , there are two main frequencies. In the case of  $Gr = 7.5 \times 10^6$ , the frequencies

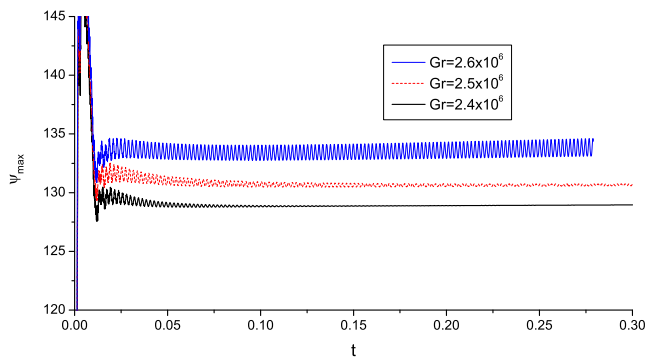


Fig. 3. The oscillation of  $\psi_{max}$  in cases of  $Gr = 2.4 \times 10^6$ ,  $2.5 \times 10^6$ , and  $2.6 \times 10^6$ .

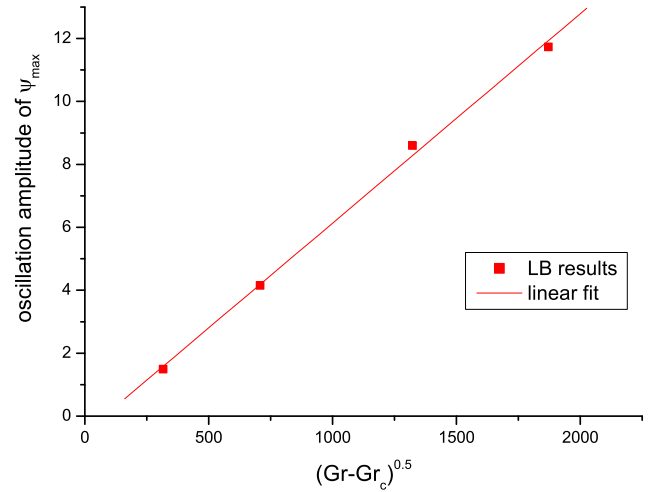


Fig. 4. The oscillation amplitude  $\psi_{max}$  as a function of  $(Gr - Gr_c)^{0.5}$ , where  $Gr_c$  is about  $2.5 \times 10^6$ .

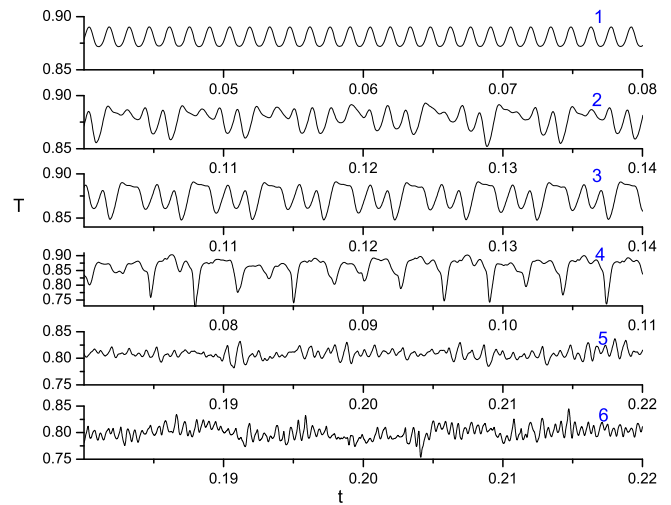


Fig. 5. Temperature oscillations at the point ( $r = 0.64, x = 0.5$ ). Curves 1–6 are obtained from cases of  $Gr = 6 \times 10^6$ ,  $7 \times 10^6$ ,  $7.5 \times 10^6$ ,  $1 \times 10^7$ ,  $3 \times 10^7$ , and  $6 \times 10^7$ .

are locked  $f_2 = \frac{f_1}{2} = \frac{f_0}{8}$ , where  $f_0 = 4903$ . Further higher  $Gr$  leads to a chaotic behavior. Thus the route to chaotic behavior is through period doubling as observed in many other complex systems.

We also plotted the contours of the average temperature and rms amplitude of temperature oscillations for the largest Grashof number  $Gr = 6 \times 10^7$  in Fig. 6. The rms amplitude of the temperature oscillations is defined as

Table 5  
Frequency of the flows in the periodic regime.

Gr	Frequency	Frequency [2]
$2.5 \times 10^6$	3047	3140
$2.6 \times 10^6$	3082	–
$3.0 \times 10^6$	3275	–
$4.3 \times 10^6$	3792	–
$6.0 \times 10^6$	4356	4320
$7.0 \times 10^6$	1135, 4705	1100, 4670
$7.5 \times 10^6$	Locked $f_2 = \frac{f_1}{2} = \frac{f_0}{8}$ where $f_0 = 4903$	Locked $f_2 = \frac{f_1}{2} = \frac{f_0}{8}$ where $f_0 = 4880$

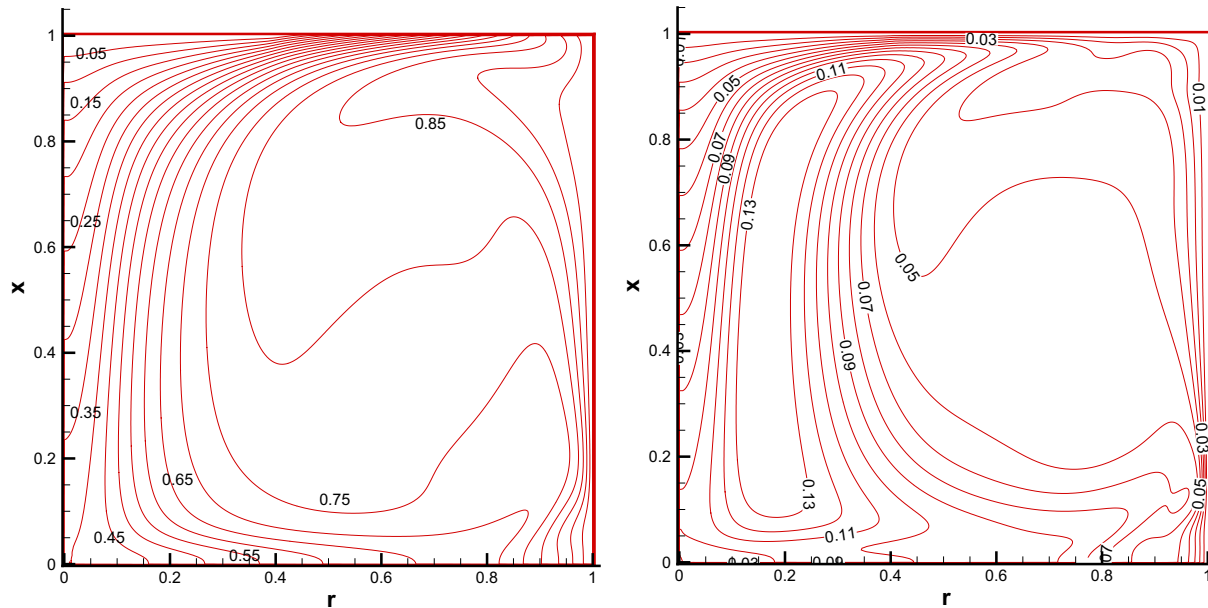


Fig. 6. (a) Contours of the average temperature and (b) rms amplitude of temperature oscillations at the flow  $Gr = 6 \times 10^7$ .

$$T_{rms}(x, r) = \langle (T(x, r, t) - \langle T(x, r, t) \rangle)^2 \rangle^{0.5} \quad (16)$$

where the symbol  $\langle \rangle$  implies the averaging over the whole time interval. The distributions of these mean quantities at such high Grashof number is found still similar to those obtained by 3D simulations [2].

In this section, we observed the typical flow patterns in the oscillation regimes. These observations and frequency analysis agree well with the study of Nikitin et al. [2] who obtained their results from a spectral-finite-difference method.

## 5. Conclusions

A lattice Boltzmann scheme has been applied to solving melt flows in the CZ crystal growth system. Not only the NS equations are solved by the LBM, but also the equation for swirling velocity and the heat equation. It is more consistent in methodology and has better numerical stability than hybrid schemes [5,6]. As a result, this scheme can give results for high Reynolds number and high Grashof number cases with smaller grid size.

Through study on the flows with high Grashof number, the transition from steady flow to periodic flow is found to be occur at about  $2.5 \times 10^6$ . The oscillation amplitude  $\psi_{max}$  is proportional to  $(Gr - Gr_c)^{0.5}$  for  $2.5 \times 10^6 < Gr < 6 \times 10^6$ . This conclusion agrees well with the study of Nikitin et al. [2]. The frequencies of the unsteady flow we obtained also seem correct. The distributions of the mean quantities of the temperature and rms of temperature at high Grashof number are found to be similar to the 3D results in Ref. [2]. The axisymmetric simulations are still useful to predict the real 3D melt flow in CZ crystal growth in such a high Grashof number.

## Acknowledgments

This work was partially supported by the Alexander von Humboldt Foundation, Germany. Grant for Excellent Youth University Teacher in Anhui Province, China.

## References

- [1] U. Buckle, M. Schafer, Benchmark results for the numerical simulation of flow in Czochralski crystal growth, *J. Cryst. Growth* 126 (1993) 682–694.
- [2] N. Nikitin, V. Polezhaev, Direct simulations and stability analysis of the gravity driven convection in a Czochralski model, *J. Cryst. Growth* 230 (1–2) (2001) 30–39.
- [3] D. Xu, C. Shu, B.C. Khoo, Numerical simulation of flows in Czochralski crystal growth by second-order upwind QUICK scheme, *J. Cryst. Growth* 173 (1–2) (1997) 123–131.
- [4] I. Raspo, J. Ouazzani, R. Peyret, A spectral multidomain technique for the computation of the Czochralski melt configuration, *Int. J. Numer. Methods Heat Fluid Flow* 6 (1) (1996) 31–58.
- [5] Y. Peng, C. Shu, Y.T. Chew, J. Qiu, Numerical investigation of flows in Czochralski crystal growth by an axisymmetric lattice Boltzmann method, *J. Comput. Phys.* 186 (1) (2003) 295–307.
- [6] H.B. Huang, T.S. Lee, C. Shu, Hybrid lattice-Boltzmann finite-difference simulation of axisymmetric swirling and rotating flows, *Int. J. Numer. Methods Fluids* 53 (11) (2007) 1707–1726.
- [7] H.N. Dixit, V. Babu, Simulation of high Rayleigh number natural convection in a square cavity using the lattice Boltzmann method, *Int. J. Heat Mass Transfer* 49 (3–4) (2006) 727–739.
- [8] H. Huang, T.S. Lee, C. Shu, Lattice-BGK simulation of steady flow through vascular tubes with double constrictions, *Int. J. Numer. Methods Heat Fluid Flow* 16 (2) (2006) 185–203.
- [9] I. Halliday, L.A. Hammond, C.M. Care, K. Good, A. Stevens, Lattice Boltzmann equation hydrodynamics, *Phys. Rev. E* 64 (2001) 011208.
- [10] J.G. Zhou, Axisymmetric lattice Boltzmann method revised, *Phys. Rev. E* 84 (3) (2011) 036704.
- [11] Q. Li, Y.L. He, G.H. Tang, W.Q. Tao, Improved axisymmetric lattice Boltzmann scheme, *Phys. Rev. E* 81 (5) (2010) 056707.
- [12] Z. Guo, H. Han, B. Shi, C. Zheng, Theory of the lattice Boltzmann equation: lattice Boltzmann model for axisymmetric flows, *Phys. Rev. E* 79 (4) (2009) 046708.
- [13] H.B. Huang, X-Y Lu, Theoretical and numerical study of axisymmetric lattice Boltzmann models, *Phys. Rev. E* 80 (2009) 016701.
- [14] R.G.M. van der Sman, Galilean invariant lattice Boltzmann scheme for natural convection on square and rectangular lattices, *Phys. Rev. E* 74 (2006) 026705.
- [15] H.W. Zheng, C. Shu, Y.T. Chew, A lattice Boltzmann model for multiphase flows with large density ratio, *J. Comput. Phys.* 218 (1) (2006) 353–371.
- [16] P.H. Kao, R.J. Yang, Simulating oscillatory flows in Rayleigh–Benard convection using the lattice Boltzmann method, *Int. J. Heat Mass Transfer* 50 (17–18) (2007) 3315–3328.
- [17] T. Inamuro, A lattice kinetic scheme for incompressible viscous flows with heat transfer, *Philos. Trans. R. Soc. London Ser. A* 360 (1792) (2002) 477–484.
- [18] C. Huber, A. Parmigiani, B. Chopard, M. Manga, O. Bachmann, Lattice Boltzmann model for melting with natural convection, *Int. J. Heat Fluid Flow* 29 (5) (2008) 1469–1480.
- [19] S. Chen, J. Tölke, M. Krafczyk, Numerical simulation of fluid flow and heat transfer inside a rotating disk–cylinder configuration by a lattice Boltzmann model, *Phys. Rev. E* 80 (2009) 016702.

- [20] A.A. Wheeler, 4 Test problems for the numerical simulation of flow in Czochralski crystal growth, *J. Cryst. Growth* 102 (4) (1990) 691–695.
- [21] E. Bansch, D. Davis, H. Langmach, G. Reinhardt, M. Uhle, Two- and three-dimensional transient melt-flow simulation in vapour–pressure-controlled Czochralski crystal growth, *Comput. Fluids* 35 (2006) 1400–1419.
- [22] J.R. Ristorcelli, J.L. Lumley, Instabilities, transition and turbulence in the Czochralski crystal melt, *J. Cryst. Growth* 116 (1992) 447–460.
- [23] L.D. Landau, E.M. Lifschitz, *Fluid Mechanics*, second ed., Pergamon, Oxford, 1987.
- [24] X. He, L. Luo, Lattice Boltzmann model for the incompressible Navier–Stokes equation, *J. Stat. Phys.* 88 (3/4) (1997).
- [25] X.Y. He, S. Chen, G.D. Doolen, A novel thermal model for the lattice Boltzmann method in incompressible limit, *J. Comput. Phys.* 146 (1998) 282–300.
- [26] X.Y. He, L.S. Luo, Theory of the lattice Boltzmann method: from Boltzmann equation to the lattice Boltzmann equation, *Phys. Rev. E* 56 (6) (1997) 6811–6817.
- [27] T. Inamuro, M. Yoshino, H. Inoue, R. Mizuno, F. Ogino, A lattice Boltzmann method for a binary miscible fluid mixture and its application to a heat-transfer problem, *J. Comput. Phys.* 179 (1) (2002) 201–215.
- [28] H.B. Huang, X-Y Lu, M.C. Sukop, Numerical study of lattice Boltzmann methods for a convection–diffusion equation coupled with Navier–Stokes equations, *J. Phys. A: Math. Theor.* 44 (5) (2011) 055001.
- [29] X.Y. He, Q.S. Zou, L.S. Luo, M. Dembo, Analytic solutions of simple flows and analysis of nonslip boundary conditions for the lattice Boltzmann BGK model, *J. Stat. Phys.* 87 (1–2) (1997) 115–136.
- [30] M. Bouzidi, M. Firdaouss, P. Lallemand, Momentum transfer of a Boltzmann-lattice fluid with boundaries, *Phys. Fluids* 13 (11) (2001) 3452–3459.
- [31] Q.S. Zou, X.Y. He, On pressure and velocity boundary conditions for the lattice Boltzmann BGK model, *Phys. Fluids* 9 (6) (1997) 1591–1598.
- [32] L. Chen, Qinjun Kang, Ya-Ling He, Wen-Quan Tao, Mesoscopic study of the effects of gel concentration and materials on the formation of precipitation patterns, *Langmuir* 28 (32) (2012) 11745–11754.
- [33] Q. Kang, P.C. Lichtner, D. Zhang, An improved lattice Boltzmann model for multicomponent reactive transport in porous media at the pore scale, *Water Resour. Res.* 43 (12) (2007).
- [34] Li Chen, Q. Kang, et al., Pore-scale modeling of multiphase reactive transport with phase transitions and dissolution–precipitation processes in closed systems, *Phys. Rev. E* 87 (4) (2013) 043306.